International Journal of Nanomedicine

Dovepress
open access to scientific and medical research

Open Access Full Text Article

ORIGINAL RESEARCH

Multifunctional AuPt Nanoparticles for Synergistic Photothermal and Radiation Therapy

Han Tang[1,*], Ji Chen[2,*], Lu He Qi[3], Meng Lyu[4], Hong Quan[1], Zhi Jie Tan[1]

[1]Key Laboratory of Artificial Micro- and Nano-Structures of Ministry of Education, School of Physics and Technology, Wuhan University, Wuhan, People's Republic of China; [2]Department of Radiation and Medical Oncology, Hubei Key Laboratory of Tumor Biological Behaviors, Hubei Cancer Clinical Study Center, Zhongnan Hospital of Wuhan University, Wuhan, People's Republic of China; [3]School of Resource and Environmental Sciences, Wuhan University, Wuhan, People's Republic of China; [4]Department of Gastrointestinal Surgery, Shenzhen People's Hospital (The Second Clinical Medical College, Jinan University, the First Affiliated Hospital, Southern University of Science and Technology), Shenzhen, Guangdong, People's Republic of China

*These authors contributed equally to this work

Correspondence: Hong Quan; Zhi Jie Tan, School of Physics and Technology, Wuhan University, Wuhan, Hubei Province, 430072, People's Republic of China, Email 00007962@whu.edu.cn; zjtan@whu.edu.cn

Background: Photothermal therapy (PTT) has gained considerable interest as an emerging modality for cancer treatment in recent years. Radiation therapy (RT) has been widely used in the clinic as a traditional treatment method. However, RT and PTT treatments are limited by side effects and penetration depth, respectively. In addition, hypoxia within the tumor can lead to increased resistance to treatment.

Methods: We synthesized multiple sizes of AuPt by modulating the reaction conditions. The smallest size of AuPt was selected and modified with folic acid (FA) for PTT and RT synergy therapy. Various methods including transmission electron microscope (TEM), X-ray photoelectron spectroscopy (XPS), X-ray diffraction (XRD), and Fourier transform infrared spectroscopy (FITR) are used to determine the structure and composition of AuPt-FA (AF). In addition, we researched the photothermal properties of AF with IR cameras and infrared lasers. Flow cytometry, colony formation assays, CCK8, and fluorescent staining for probing the treatment effect in vitro. Also, we explored the targeting of AF by TEM and In Vivo Imaging Systems (IVIS). In vivo experiments, we record changes in tumor volume and weight as well as staining of tumor sections (ROS, Ki67, and hematoxylin and eosin).

Results: The AuPt with particle size of 16 nm endows it with remarkably high photothermal conversion efficiency (46.84%) and catalase activity compared to other sizes of AuPt (30 nm and 100 nm). AF alleviates hypoxia in the tumor microenvironment, leading to the production of more reactive oxygen species (ROS) during the treatment. In addition, the therapeutic effect was significantly enhanced by combining RT and PTT, with an apoptosis rate of 81.1% in vitro and an in vivo tumor volume reduction rate of 94.0% in vivo.

Conclusion: These results demonstrate that AF potentiates the synergistic effect of PTT and RT and has the potential for clinical translation.

Keywords: photothermal, radiotherapy, hypoxia relief, catalase activity, microscale, synergistic effect

Introduction

Cancer is one of the deadliest diseases worldwide. For nearly a century, conventional cancer treatments such as clinical surgery, chemotherapy, and radiotherapy have been the primary modalities for cancer treatment and palliation.[1] Radiotherapy (RT) uses high-energy particles to target malignant tumors in a specific region, causing direct or indirect DNA damage to cancer cells. Metal materials with high atomic numbers can generate more free radicals under radiation due to the effects of Compton electron scattering, secondary electron scattering, and photoelectron absorption.[2,3] Therefore, nanoparticles such as Au, Pt, Pb, Ir, Ru, Bi, etc. are often used as radiosensitizers to enhance the efficacy of radiotherapy.[4–10] Photothermal therapy (PTT) is a novel modality for cancer treatment that utilizes specific materials to convert near-infrared (NIR) light into heat. By maintaining the temperature at 45–55 ^{o}C, PTT can disrupt the metabolism of cancer cells and induce cell apoptosis. This modality has good specificity and stability, which has enormous clinical

Received: 15 June 2023
Accepted: 27 October 2023
Published: 20 November 2023

Graphical Abstract

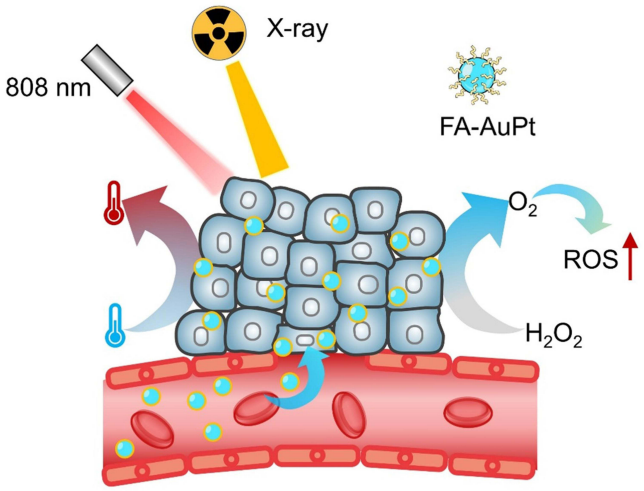

potential and has attracted considerable interest.[11,12] However, RT suffers from poor specificity and high toxicity to normal tissues adjacent to the tumor. Similarly, PTT is limited by the low penetration depth of NIR light and can only treat superficial malignant tumors.[13]

The tumor microenvironment (TME) is a unique and important characteristic of solid tumors, primarily characterized by a high concentration of glutathione and H_2O_2, as well as an acidic environment.[14] Hypoxia is another prominent feature of solid tumors, resulting from abnormal tumor metabolism and a heterogeneous vascular network. The lack of oxygen can significantly increase the resistance of cancer cells to therapy, underscoring the critical importance of providing sufficient oxygen in RT and PTT. There are many ways to address tumor hypoxia resistance, including catalyzing H_2O_2 to generate oxygen,[15] transporting oxygen to tumor cells,[16] hypoxic or low pH activated drugs,[17] and photosynthesis to generate oxygen.[18] All of these methods have achieved excellent results in tumor treatment.

Gold (Au, Z=79) and platinum (Pt, Z=78) are promising candidates for cancer treatment due to their applications in radiotherapy, drug delivery, photothermal therapy, and photodynamic therapy (PDT).[19–22] A key property of Pt is its ability to catalyze over-expressed H_2O_2 in the TME to produce O_2, thereby alleviating hypoxia.[23–26] Moreover, the combination of Au and Pt can greatly enhance the efficiency of photothermal conversion, as Pt shifts the optical absorption from the visible to the near-infrared (NIR) region through a spectral coupling effect.[27,28] Furthermore, Au and Pt exhibit lower cytotoxicity to the body, resulting in fewer side effects. Therefore, the application of AuPt alloy is extremely broad in various treatments. For example, the Wang group synthesized AuPt core-shell structures for a combination of chemotherapy and photothermal therapy,[29] while the Zhang group synthesized star-like Au/Pt enzymes for PTT and PDT.[30] Wang et al reported that the AuPtAg-GOx nanocomposites acted as nanozymes for immunotherapy and PTT,[31] and Song et al fabricated biomimetic DOX/AuPt for chemo-photothermal therapy.[32] However, to the best of our knowledge, there are few studies on AuPt nanoparticles for combined PTT and RT.

Nanoparticle size is a crucial factor that affects their function and application, including their efficiency in photothermal conversion, circulation time, catalytic efficiency, etc.[33] The size of AuPt nanoparticles also may influences their ability to catalyze H_2O_2 to O_2. Moglianetti et al demonstrated that 5 nm Pt nanoparticles have higher catalytic ability in horseradish peroxidase, catalase (CAT), and superoxide dismutase than 20 nm Pt nanoparticles at the same concentration, due to their better dispersion and specific surface area.[34] In addition, smaller nanoparticles can more easily penetrate the deep regions of solid tumours, enhancing the therapeutic effect.[35] Previous studies have synthesized AuPt nanoparticles with various sizes (30–100 nm) for different therapeutic applications.[31,36–39]

Here, we synthesized smaller AuPt nanoparticles (16nm) using a one-step method by controlling the pH value, heating temperature, proportion of composite materials, and reaction speed. Our results have shown that AuPt nanoparticles have the strongest catalytic activity compared to other sizes (30 and 100 nm) based on the rate of oxygen production in vitro. To enhance their targeting ability for RT and PTT, we have functionalized the nanoparticles with folic acid (FA) (Scheme 1). It is important to note that AuPt-FA (AF) possesses several advantages: i) It exhibits very low biological toxicity and side effects and high targeting ability; ii) Its photothermal conversion rate (46.84%) is higher than most other materials in the NIR-I window (808 nm). iii) It exhibits a brilliant energy deposition that leads to ROS improvement (77.81%) and a significant increase in lethality in tumor cells, and iv) they exhibit a synergistic effect (94.10% tumor elimination) when combined with radiotherapy and photothermal therapy.

Materials and Methods

Materials

$HAuCl_4 \cdot 3H_2O$, $H_2PtCl_6 \cdot 6H_2O$, Pluronic F127 (F127), dicyclohexylcarbodiimide (DCC), folic acid, N-hydroxysuccinimide (NHS), sulfo-cyanine3, ascorbic acid (AA) were obtained from Sigma Aldrich (Shanghai, China). Fetal bovine serum (FBS), trypsin, Phosphate buffered saline (PBS), the electron microscope fixative (2.5% glutaraldehyde) and Roswell Park Memorial Institute (RMPI) 1640 cell culture medium were obtained from Gibco (Shanghai, China). 4% Paraformaldehyde, anti-pimonidazole, antibody 4,6-diamidino-2-phenylindole (DAPI), Cell counting Kit 8 (CCK 8), crystal violet staining solution, 0.1% Triton-X100,γ-H2AX antibody, caspase 3 antibodies were purchased from Invitrogen Corp. (CA., USA). The other materials used in vivo and vitro experiments were obtained from Sinopharm Chemical Reagent (China) and Aladdin-Reagent (China).

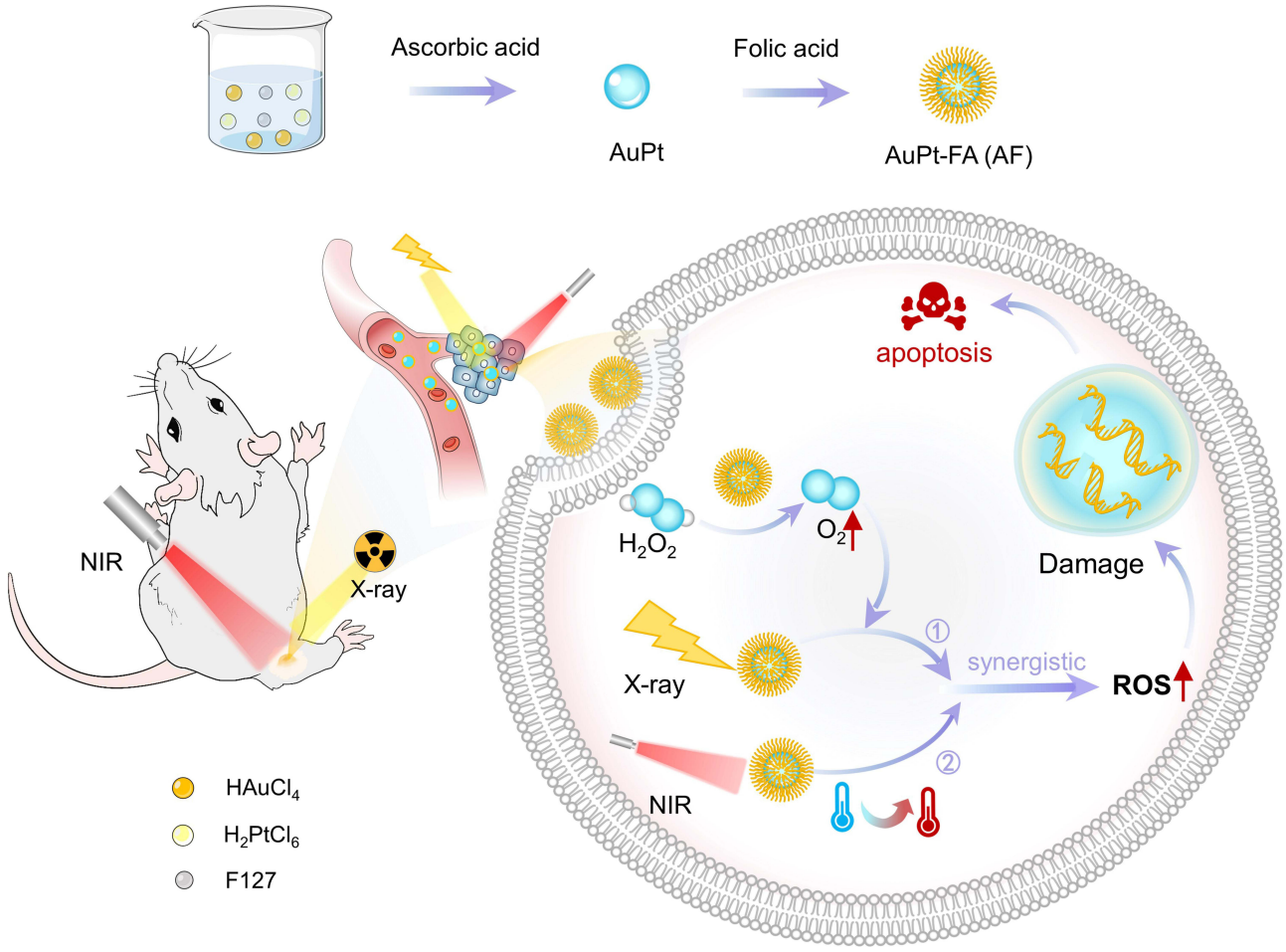

Scheme 1 Synthesis of AF and its application in alleviating hypoxia for photothermal and radiation therapy.

Material Characterization

Transmission electron microscope (TEM) (JEM-2100plus, Japan) was used to observe the morphology and structure of nanoparticles. Phase structures were acquired by X-ray diffraction (XRD) (Bruker, XPert Pro, Netherlands). X-ray photoelectron spectroscopy (XPS) (ESCA-LAB250Xi, Thermo Fisher Ltd., USA) was used to analyze element composition. The zeta potential of nanoparticles was obtained by dynamic light scattering (DLS) (Zetasizer Nano ZSP, Malvern Instruments, UK). Characteristic peak analysis using Fourier transform infrared spectroscopy (FTIR) (Nicolet 5700, Thermo Fisher Ltd., USA). The optical absorbance of nanoparticles was measured by UV-visible-NIR spectrophotometer (UV-2550, Shimadzu, Japan). The concentration of gold and platinum was analyzed on ICP-MS (7500a, Agilent Technology Ltd., USA).

Synthesis of AF

The AuPt nanoparticles were prepared in one step: Briefly, 1.0 mL of H_2PtCl_6 (10 mM) solution and 1.0 mL of $HAuCl_4$ (10 mM) were mixed with 40 mL DI water and 0.015 g of Pluronic F127 in a 50 mL glass bottle. The solution was sonicated for 20 min and NaOH (1 M) was added to adjust the pH. Afterwards, AA solution (0.5 mL, 0.6 M) was added and stirred for 3 h. After aging for 24 h, products were collected by centrifuge at 16,000 rpm for 5 min. The collected black materials were washed with DI water and ethanol three times before being dried. Keep the ratio of Au and Pt unchanged, and obtain AuPt of other sizes (30,100 nm) by changing the values of F127 and pH.

To successfully couple folic acid to AuPt, folic acid (60 mg), DDC (25 mg) and sulfo-NHS (25 mg) were mixed with 40mL of ethanol stirred overnight in dark for 48 h. Afterwards, AuPt (50 mg) was added to the solution and continued to stir and ultrasonic. After aging for 10 h, materials were dialyzed and collected. Before completing experiments and tests, the material is stored away from light.[40]

O_2 Catalyze Measurements of AF

The ability of materials in O_2 generation was investigated. H_2O_2 (3.2 mM) and AF (100 μg/mL) were dissolved in 5 mL of PBS. An oxygen probe (DOG-3082 oxygen dissolving meter) was used to monitor the generation of oxygen every minute.

In vitro Photothermal Performance Studies

AF with different concentrations (0, 12.5, 25, 50, and 100 μg/mL) dispersed in PBS was irradiated by an 808 nm laser with the energy density of 1.0 W/cm^2. The temperature was recorded by an IR camera thermal graphic system (HBT-2A, Hao Bo Technology, China), and the time interval for each observation was 30s. Besides, the temperature change was monitored for the same concentration (100 μg/mL) at different energy densities (0.75, 1, 1.5 and 2 W/cm^2). Then, the ON/OFF cycle irradiation experiment was completed to test the stability of AF photothermal conversion. The AF (100 μg/mL) solution was irradiated by laser (808 nm, 1 W/cm^2, 5 min), and data were recorded when the solution cooled down to room temperature. This cycle was repeated 6 times.

Cell Culture

The 4T1 (mouse breast cancer cell line) purchased commercially from the Cell Bank of the Chinese Academy of Sciences were selected for cell experiments. The 4T1 cells were cultured in medium 1640 with 10% fetal bovine serum, 1% antibiotics (penicillin-streptomycin, 10,000 U/mL$^-$) at 37 °C in a proper atmosphere with 5% CO_2. The cells were seeded into 96-well or 6-well plates for different vitro experiments.

Cellular Uptake and Cytotoxicity of AF in vitro

To study the intracellular uptake of AF, cells (10^6 cells per well) were incubated in 6-well for 24 h and then cultured with AF or AuPt for 4 h. Then, the medium was removed and the electron microscope fixative (2.5% glutaraldehyde) was added for 10 min. The cells were collected and scraped from the culture dish by cell scraping. After centrifugation (1000 r/min, 5 min) and removal of the supernatant, 2 mL new electron microscope fixative was added and the cells were continuously fixed for 2h at room temperature, and finally observed by microscope.

The apoptosis situation and cytotoxicity were studied. 5×10^5 4T1 cells were cultured in 6-well for 24 h. Afterwards, cells were cultured with different concentrations of AF (0, 50, 100, 150, and 200 μg/mL) for 24 h. Subsequently, cells were harvested and collected by centrifuging (2000 rpm, 5 min). After cells being washed three times with PBS and dispersed in 500 μL binding buffer, Annexin V-FITC and PI were used to stain cells. Cell viability was analyzed by a flow cytometer (cytoFlex S, BECKMAN, USA).

Colony Formation Assay

The long-term toxicity of different concentrations of AF to cells and the radiosensitivity enhancement ability were investigated through cloning formation assay. 4T1 cells (1000 cells per well) were seeded in 6-well plates and treated by AF (0, 50, 100, and 200 μg/mL) for 5 h. After being treated by ionizing radiation (6 Gy), cells continuously were cultured for 8 days with the new medium. Finally, crystal violet was used to stain the cell clone cluster. The survival fraction is obtained by counting the number of cell clones and comparing it with the control group.

Synergistic Therapeutic Effects in vitro

To study survival rate and combine therapy performance. About 2×10^3 4T1 cells per well were seeded in 96-well plates for 24 h. Cells were treated by AF (0, 50, 100, 150, and 200 μg/mL) and irradiated with or without 808nm laser (1 W/cm^2, 5 min) and X-ray (6 Gy). After treatment for 24 h, 10 μL of CCK 8 was added and incubated for 2 h. UV–visible–NIR spectrophotometer was used to analyze the optical density (OD) at 450 nm, and the survival rate was calculated according to the formula:

$$\text{Cell viability} = \left(OD_{\text{Experimental group}} - OD_{\text{Blank}}\right)/\left(OD_{\text{Control}} - OD_{\text{Blank}}\right)\times 100\% \quad (1)$$

DNA Damage and Live/Dead Stain

4T1 cells were cultured in 24-well plates for 24 h at 37 °C. Cells were treated with (i) PBS, (ii) RT (6 Gy), (iii) AF, (iv) AF+NIR (808 nm,1 W/cm^2,5 min), (v) AF+RT, (vi) AF+RT+NIR. After different treatments for 3 h, the cells were fixed by paraformaldehyde for 15 minutes and washed with PBS three times, then treated with 0.2% Triton X for 5 min and washed with PBS three times again. The cells were treated with 5% BSA as a block buffer for 2h. Finally, diluted DAPI (1:500) and γ-H_2AX antibodies were used to stain cells. Images were observed and analyzed through a fluorescence microscope (IX81) and the software ImageJ. Also, Calcein-AM/PI was applied to stain live/dead cells.

Flow Cytometry Measurements for ROS

4T1 cells (10^6 cells per well) were incubated in 6-well for 24h. After being treated by medium with AF (100 μg/mL) for 4 h, cells were divided into 6 groups: (i) Control, (ii) RT, (iii) AF, (iv) AF+NIR, (v) AF+RT, (vi) AF+RT+NIR. After treatment with or without X-ray (6 Gy) and 808 nm laser (1 W/cm^2,5 min) for 30 min, cells were incubated with 20,70-dichlorofluorescein diacetate (DCFH-DA) solution (10 μM) after collected. Serum-free medium was used to wash the residue DCFH-DA three times. Finally, the generation of ROS was recorded by a flow cytometer.

Establish of Subcutaneous Tumour-Bearing Model

4T1 tumor model was established in female BALB/c mice aged 4–5 weeks and purchased from Vital River Company (Beijing, China). All vivo experiments were proved by Wuhan University Animal Care Facility and National Institutions of Health Guidelines. 100 μL of PBS containing 1×10^7 4T1 cells were subcutaneously injected into the left hind leg of mice.

In vivo Target and Photothermal Effect

When tumors reached 80 mm^2,1mg/mL Cy3-AF and Cy3-AuPt were dissolved in 100uL PBS and injected intravenously. After 12 hours, the IVIS system (PerkinElmer IVIS Lumina LT Series III) was used to detect the distribution of materials in mice.To test the photothermal effect in vivo, two groups of mice with different treatments (100 μL PBS,100 μL AF (1 mg/mL)) were irradiated (808 nm, 1 W/cm^2,5 min) and temperature changes are recorded by IR camera.

In vivo Antitumor Experiment

After the tumor volume reached about 200 mm^3, all mice were separated into 5 groups (5 mice per group): (i) PBS (Control), (ii) RT, (iii) NDs + NIR, (iv) NDs + RT, (v) NDs + NIR + RT. The PBS (200 μL) and 1 mg/mL of AF (200 μL) were injected into the tail vein. After 24 h, the mice of the group (ii) and (v) were irradiated by a laser (808 nm, 1 W / cm^2, 5 min) and the mice of the group (ii), (iv) and (v) were treated by X-ray (6 Gy). Subsequently, Body weight and tumor volume were recorded every 3 days, the formula was used to calculate tumor volume: tumor volume = tumor length×tumor $width^2/2$.

In addition, to detect ROS production in tumor cells, the fluorescent dye DHE (10 μM, 50 μL) was injected intravenously into mice. The mice were sacrificed on the 19^{th} day after various treatments. The blood and various organs including heart, liver, spleen, lungs and kidneys of mice were collected and analyzed. Tumour samples were collected and stored in paraffin. After tumors were cut into thick sections, hematoxylin and eosin (H&E) staining, Ki67 detection, and ROS staining analysis were used to observe the effect of treatment and toxicity on mice.

Statistical Analysis

Data analyses were conducted using the GraphPad Prism 8.0 software. Significance between every two groups was calculated by the Student's *t*-test. *P < 0.05, **P < 0.01, ***P < 0.005.

Result and Discussion

Synthesis and Characterization of AF

Nanoscale AuPt was obtained through a one-step synthesis. Briefly, F127 was used as a growth template, and AA was used as a reducing agent to reduce $HAuCl_4$ and H_2PtCl_6.[41] By adjusting the concentration, stirring speed, temperature, and pH value, small AuPt nanoparticles were obtained, with sizes mostly ranging from 12 nm to 24 nm and an average diameter of 16 nm, as shown by transmission electron microscopy (TEM) (Figure 1a) and size distribution statistics (Figure 1b). Moreover, High-resolution TEM images revealed lattice fringes with interplanar spacings of 0.236 nm for Au (111) and 0.201 nm for Pt (200), indicating a face-centered cubic (fcc) structure. Additionally, the electron scanning mapping diagram (Figure 1c) showed that Au and Pt were uniformly distributed throughout the material, rather than forming a similar core-shell structure.[42,43] Energy dispersive X-ray spectrometry (EDX) indicated that the mass percentage of Au and Pt was approximately 60.78% and 39.22%, respectively (Figure S1).

X-ray photoelectron spectroscopy (XPS) images (Figures 2a,b and S2) showed peaks at 87.7 eV ($4f_{5/2}$), 84.0 eV ($4f_{7/2}$) of Au element and at 74.6 eV ($4f_{5/2}$), 71.3 eV ($4f_{7/2}$) for the Pt element. According to X-ray power dispersion (XRD), the peaks of Pt ((111), (200), (220)) and Au ((111), (200), (220), and (311)) are clearly shown in Figure 2c, consistent with the standard values. During the preparation process, folate was activated and connected to AuPt through a reaction with DCC and sulphur-NH_2. After centrifugation and freeze-drying, the resulting product, AF, was obtained and stored. To confirm the successful connection of FA ligands to AuPt, we compared the characteristic peaks of AF, FA, and AuPt using Fourier transform infrared (FTIR) spectroscopy. Folic acid has a benzene ring structure that typically exhibits 2–4 absorption peaks between 1450 cm^{-1} and 1600 cm^{-1}. Figure 2d shows that AF has corresponding absorption peaks, indicating the successful modification of FA. The zeta potential of AuPt changed from –16.66 eV to –20.17 eV after FA modification (Figure 2e), indicating the successful attachment of FA (–48.3 eV). The higher zeta potential implies a stronger repulsive force between nanoparticle surfaces and a more uniform dispersion in solution. We compared the changes in AuPt and AF solution before and after adding PBS solution for 24 h and observed that the folate ligand effectively promoted the dispersion of nanoparticles in PBS (Figure S3). From the images, it is evident that the AuPt group quickly aggregated in the PBS, forming a visible block and precipitating to the bottom of the glass bottle. This would reduce the catalytic and photothermal functions of the nanoparticles. In contrast, the AF solution remained stable in PBS. The UV-vis absorption spectrum (Figure 2f) at 300–900 nm with varying concentrations of AF (25, 50, 100, and 200 μg/mL) displayed a strong and flat light absorption spectrum, particularly at 808 nm, which is the laser wavelength

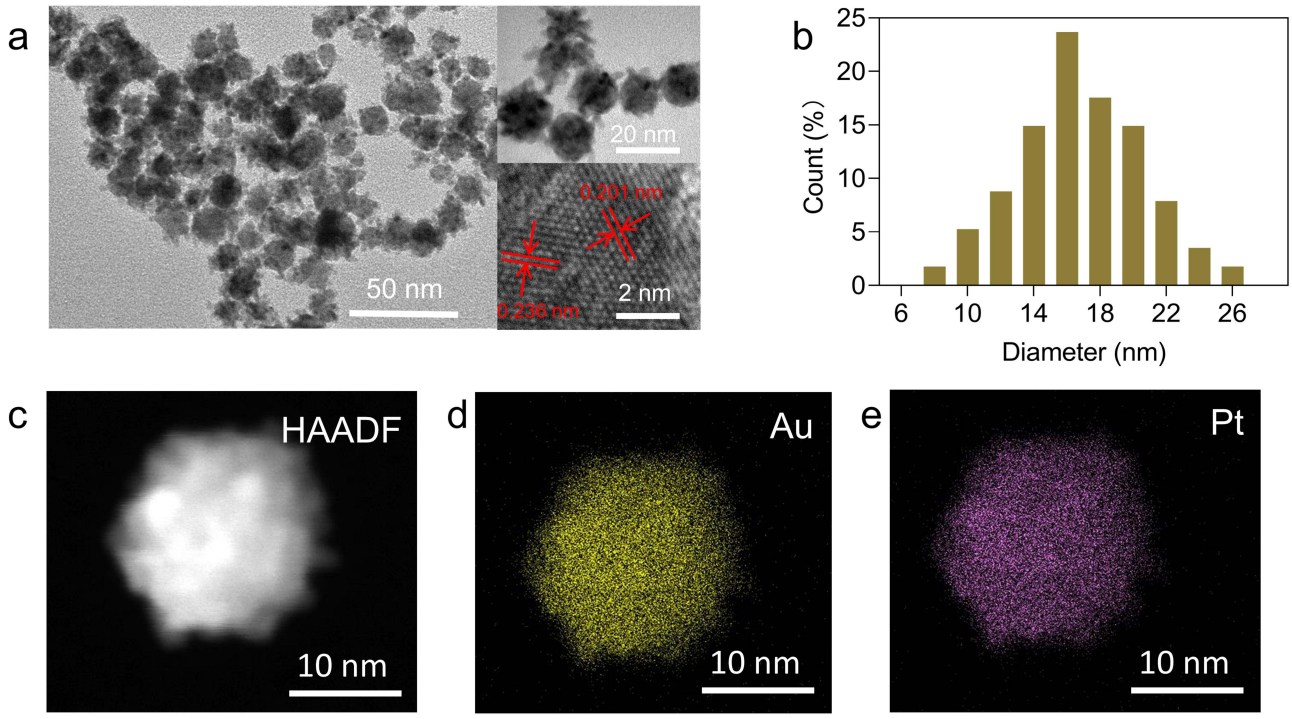

Figure 1 (**a**) TEM and HRTEM image of AuPt. (**b**) Statistical graph displaying the measured diameter of AuPt. (**c**–**e**) Element mapping image of AuPt nanoparticles.

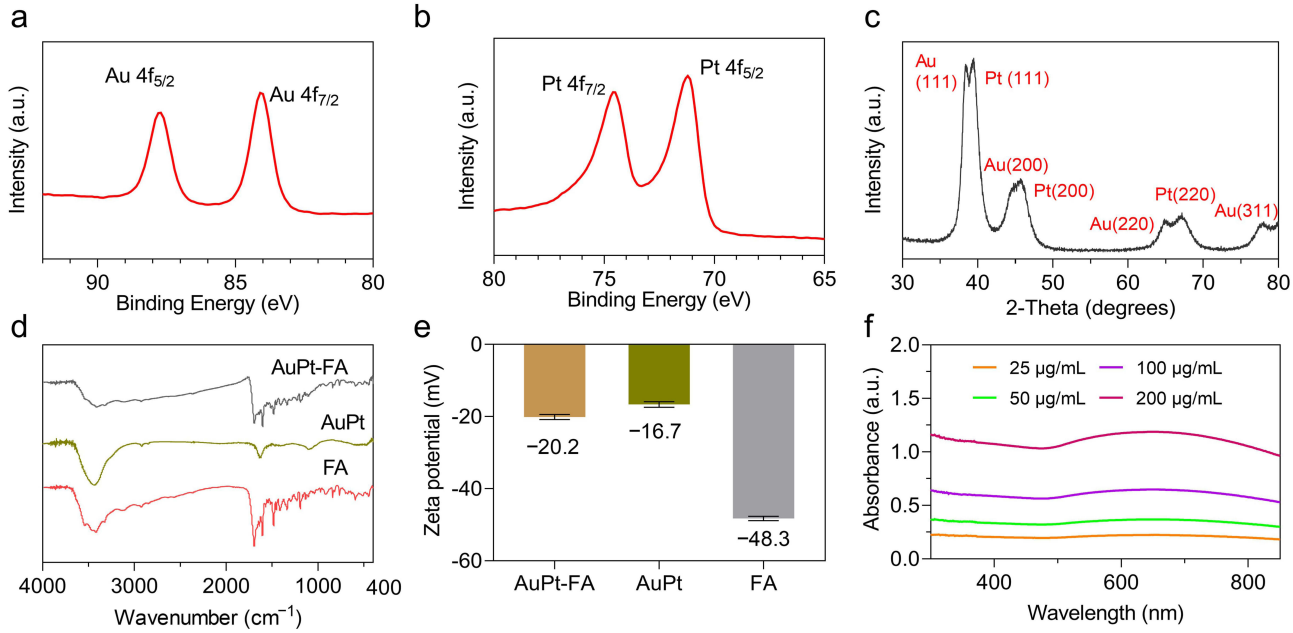

Figure 2 (**a** and **b**) XPS spectra in the Au 4f and Pt 4f regions. (**c**) XRD patterns of AuPt. (**d**) FTIR spectra of AuPt-FA, AuPt and FA. (**e**) Zeta potential of AuPt, AuPt-FA, and FA. (**f**) Concentration-dependent UV–vis–NIR absorption of AF.

selected for photothermal therapy. Higher light absorption results in a more efficient conversion of light energy into heat energy, which is more effective in killing cancer cells.[44]

The ability of AuPt nanoparticles with different sizes to catalyze H_2O_2 to generate O_2 was investigated. We obtained AuPt nanoparticles of about 30 and 100 nm by varying the concentration, pH value, and composite materials, as shown by TEM images (Figure S4a and c). The EDS diagrams (Figure S4b and d) revealed that the Pt content in AuPt (30 nm)

and AuPt (100 nm) was about 38.33% and 32.74%, respectively, which were lower than the 39.22% of AuPt (16 nm). We then measured the oxygen generation rate of 100 μg/mL of AuPt nanoparticles of different sizes in 10 mM H_2O_2 using a portable dissolved oxygen meter as indicated in Figure 3a. We observed significant differences in the catalytic enzyme activity among the three sizes of materials. After 10 min of reaction, 100 μg/mL of AuPt (16, 30, and 100 nm) respectively catalyzed H_2O_2 to produce about 10.87, 13.91, and 15.8 mg/L oxygen, with no significant change in the control group. These results indicate that AuPt (16 nm) exhibited the highest catalase-like activity, which could be attributed to its larger surface area and higher Pt content.[45] Moreover, we explored the catalase-like activity of 16 nm AuPt with different concentrations (0, 50, and 100 μg/mL), and the results are presented in Figure 3b, which indicated that higher concentrations resulted in faster O_2 production.

Photothermal Conversion in vitro

We further investigated the photothermal capacity of AF in vitro. AF samples with varying concentrations (0, 12.5, 25, 50, and 100 μg/mL) were irradiated with an 808 nm laser for 7 min (1 W/cm^2), and the temperature changes over time were recorded using infrared cameras (Figure 3c). The result showed rapid and concentration-dependent temperature increases, followed by gradual plateaus due to heat dissipation. After 7 min, the temperature increased by 25.7, 18.5, 12.9, and 6.9 °C, for the groups with different concentrations, while the control group displayed almost no temperature change. Additionally, we tested the speed of temperature increase of AF under different light powers (0, 0.75, 1, 1.5, and 2 W/cm^2). The temperature slowly rose to 10 °C with 0.75 W/cm^2 power irradiation and quickly rose to 49.5 °C with 2 W/cm^2 power, as shown in Figure S5. High power radiation led to a faster temperature rise. To assess the photothermal stability of AF, we subjected the material to 6 heat/cool cycles, with each cycle lasting for 13 min. The temperature change curve in each cycle was consistent, as shown in Figure 3d, indicating that the material was stable under an 808 nm laser. U sing the calculation formula of photothermal conversion and the absorbance of AF at 808 nm, we obtained a photothermal conversion rate of 46.84% based on the material cooling curve (Figure 3e and f).[46,47] This value was higher compared to larger AuPt nanoparticles (44.2% for ~30 nm and 41.3% for ~100 nm),[28,29] as well as most other materials such as Au (38.5%),[48] black phosphorous (BP) (24.9%),[49] and Ni_2S (43.8%),[50] etc. Overall, these findings

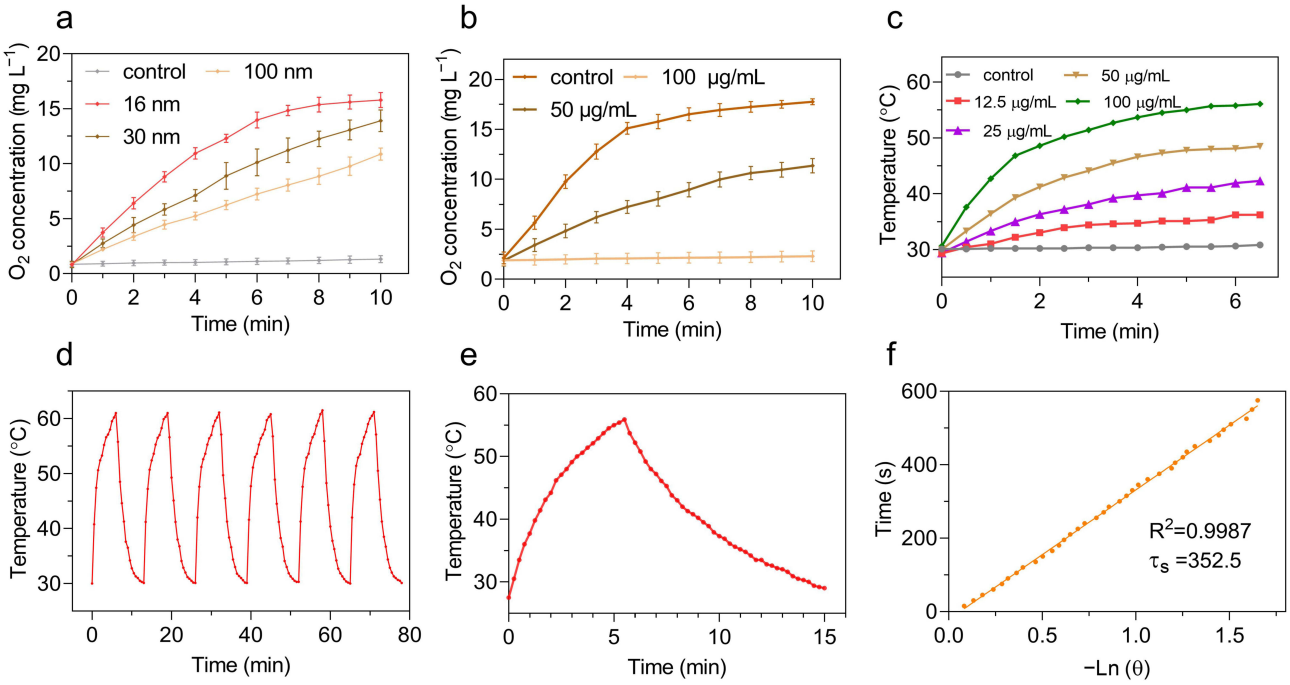

Figure 3 (**a**) Oxygen generation in H_2O_2 solution (10 mM) with AuPt of different sizes at pH 6.75. Data points represent mean ± s.d. (n = 3). (**b**) Oxygen generation in H_2O_2 solution (10 mM) using different concentrations of AuPt nanoparticles. Data points represent mean ± s.d. (n = 3). (**c**) Temperature increases of AF solutions under NIR irradiation (808 nm, 1 W/cm^2, 7 min). (**d**) Six on/off cycles of NIR laser irradiation. (**e** and **f**) Heating and cooling curves and linear fitting of AF.

demonstrate that AF possesses exceptional photothermal conversion and stability for PTT, indicating its potential for killing tumor cells.

Cellular Uptake and Cytotoxicity of AF in vitro

After successfully synthesizing AF, we investigated its cellular uptake and cytotoxicity at various concentrations in vitro. To verify the targeting ability of AF to tumor cells, we cultured AF and AuPt (50 μg/mL) with 4T1 cells for 4h. The resulting microscope images (Figure 4a and b) revealed that more nanoparticles were present around the cells in the AF group compared to the AuPt group. Next, 4T1 cells were treated with varying concentrations of AF (0, 50, 100, 150, and 200 μg/mL) for 24 h, followed by staining with Annexin V-FITC/PI Apoptosis Detection Kit, and analysis by flow cytometry. As illustrated in Figure 4c, AF exhibited excellent biological compatibility at various concentrations. Even when cultured with 200 μg/mL of AF, the cells maintained an 82.49% survival rate.

Therapeutic Effects of RT and PTT in vitro

We performed colony formation assays to determine the radiosensitizing effect of AF nanoparticles in the long term. We investigated the effect of different concentrations of AF (0, 50, 100, 200 μg/mL) on cell proliferation and radiosensitivity enhancement under 6 Gy radiation. Figures 4d and S6 illustrates that AF nanoparticles had no significant effect on cell

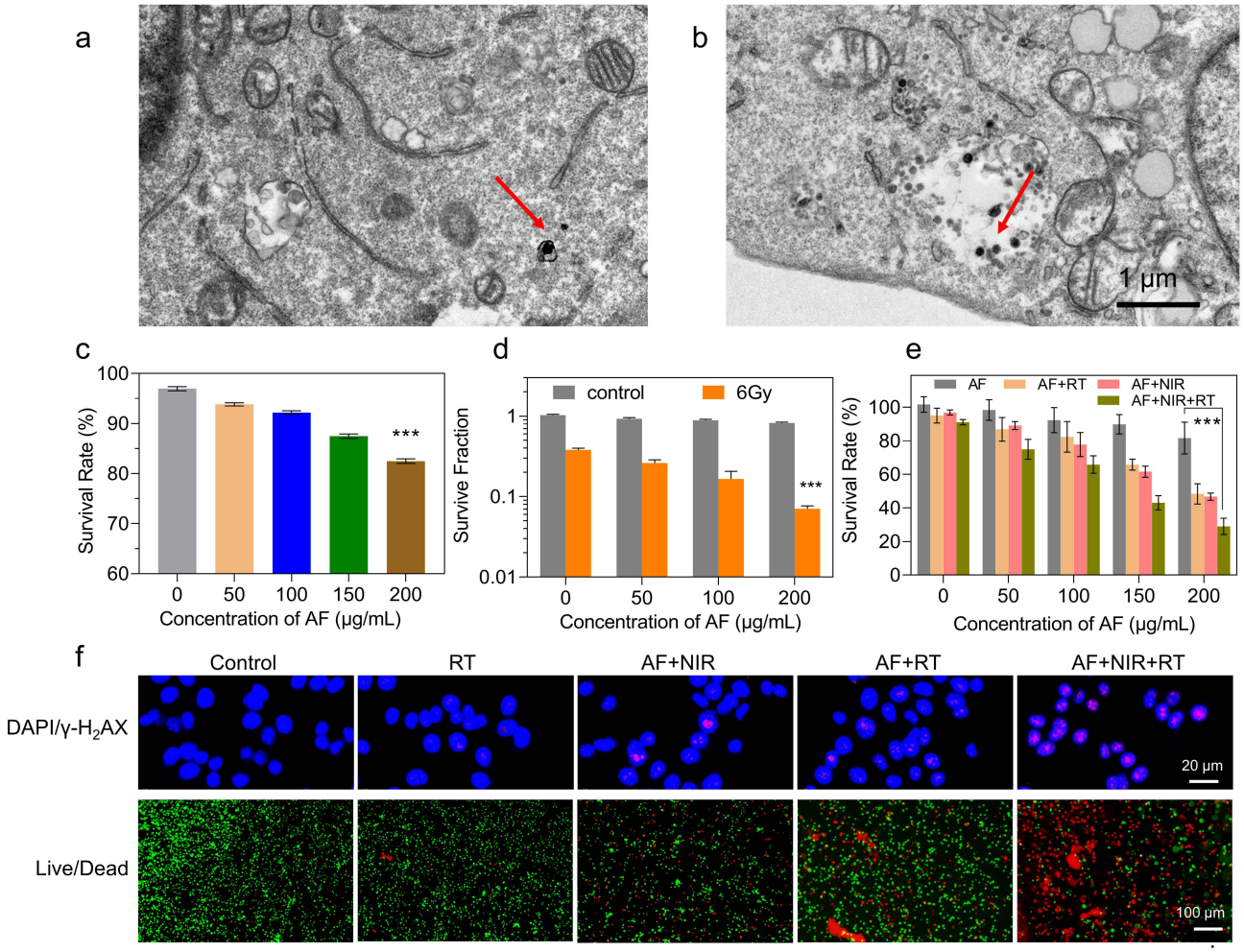

Figure 4 (**a** and **b**) The TEM micrographs after a 4h incubation with AuPt and AF. (**c**) the survival rate of 4T1 cells after being cultured with different concentrations of AF. Data points represent mean ± s.d. (n = 3). (**d**) Clonogenic cell survival fraction of 4T1 cells after exposure to different concentrations of AF and RT (6Gy). Data points represent mean ± s.d. (n = 3). (**e**) Cell viability of 4T1 cells after different treatments for 24 h. Data points represent mean ± s.d. (n = 5). (**f**) Fluorescence staining diagram of DAPI/γ-H_2AX and Live/Dead after different treatments. The nuclei were stained with DAPI (blue), DSBs were stained with γ-H_2AX (red), and live cells were stained green, while dead cells were stained red. Statistical significance was evaluated using an unpaired Student's *t*-test. ***p < 0.001.

proliferation without radiation. However, it reduced the colony formation rate of irradiated cells in a concentration-dependent manner. After 6 Gy irradiation, the cell colony formation rate was 25.3%, 16.1%, and 6.8%, respectively, corresponding to each concentration. Compared with the only RT group (38.0%), the survival rate was reduced by 33.5%, 57.7%, and 82.9%, demonstrating a significant improvement in long-term treatment efficacy by AF.

We then performed CCK8 assays to further investigate the effect of photothermal and radiotherapy at different concentrations (0, 50, 100, 150, and 200 μg/mL), and treatment methods (AF, AF+RT, AF+NIR, and AF+NIR+RT). As shown in Figure 4e, even at a low concentration of 50 μg/mL, AF significantly increased lethality compared with the control group, from 95.0% to 86.7% (RT), from 96.9% to 89.1% (NIR), and from 91.1% to 74.9% (RT+NIR). Remarkably, at a concentration of 200 μg/mL, AF exhibited a significant therapeutic effect with about 80% of cancer cells killed only one day after RT and NIR treatment, demonstrating a synergistic therapeutic effect with great potential for medical application.

To investigate the damage within cells, we used immunofluorescence staining and fluorescence microscopy to examine the synergistic effect of AF on RT and PTT. DNA double-strand (DBS) breaks play a significant role in DNA damage, and are the main reason for inducing cell apoptosis. The degree of DBS breaks in cells was qualitatively analyzed by measuring the intensity of γ-H_2AX, while the nucleus was stained with DAPI. As shown in Figure 4f, the signal of γ-H_2AX in the RT group did not change significantly, indicating low damage after only RT. In contrast, strong fluorescent signals were observed in the RT+PTT synergistic group, indicating that the nanoparticles effectively damaged DNA in the target cells as radiosensitizers and photothermal agents. To better visualize the effect of different treatment methods for AF, live/dead cells were stained with calcein (AM)/propidium iodide (PI). The staining results also demonstrated the synergetic therapeutic effect of AF.

The probe DCFH-DA test also demonstrated the same results, showing the ROS produced in cells after various treatments of AF (100 μg/mL), including control, AF, RT, AF+NIR, AF+RT, and AF+NIR+RT. ROS plays an extremely important role in cell metabolism and growth and is closely related to cell senescence, reproduction, and death. Excessive ROS can result in excessive oxidation of cells, DNA damage, and metabolic dysfunction, eventually leading to cell death.[51] The size and shape of the peak indicated that the ROS in cells had significantly improved compared to the control group after treatment with RT (7.12%) and AF+RT (12.66%) (Figure S7). Upon calculation, it can be deduced that the increase in ROS increased by 77.81% with AF treatment. In addition, the ROS of the AF+RT+PTT group increased by 26.64%, exceeding the sum of AF+RT and AF+PTT (23.11%), suggesting that RT and PTT had a synergistic effect of 1+1 greater than 2 under certain conditions.

In vivo Targeting and Photothermal Effect

To investigate AF targeting in mice, Cy3 was labeled with AF and AuPt and injected intravenously. After 12 h, we observed the AF signal in the tumour area using IVIS imaging (Figure 5a). The AF signal was approximately twice as strong as that of AuPt, indicating excellent in vivo targeting. To confirm AF accumulation in the tumor and its photothermal effect in vivo, AF (1 mg/mL) was intravenously injected into the tail of mice and PBS into the control group. After irradiation, the temperature of the tumor area in the AF group rose significantly, from 23 °C to 50 °C for 5 min, compared to that in the control group (Figure 5b). These results confirm AF's targeting and photothermal effect in vivo.

In vivo RT and PTT Synergistic Treatment

To further investigate the therapeutic effect of AF in vivo, we established BALB/c mouse tumor models. Tumour size and body weight, which reflect the health of mice, were recorded daily (Figure 5c and d). As shown in Figure 5d, the tumor volume of the control group increased rapidly from 207 mm^3 to 1449 mm^3, a seven-fold increase by day 19. Moreover, the RT group showed weak tumor growth inhibition (with a ratio of 79.1% compared to the control group) compared with the AF+RT and AF+NIR groups, which had inhibition rates of 54.5% and 55.5%, respectively. These results demonstrate that AF can enhance the effects of both radiotherapy and photothermal therapy in vivo. However, although AF significantly enhanced tumor damage during RT or NIR treatment, the tumor volume still increased slowly. Notably, after RT and PTT synergistic treatment, the tumor volume was only about 87.4 mm^3, equivalent to a 6.0% reduction compared to the control

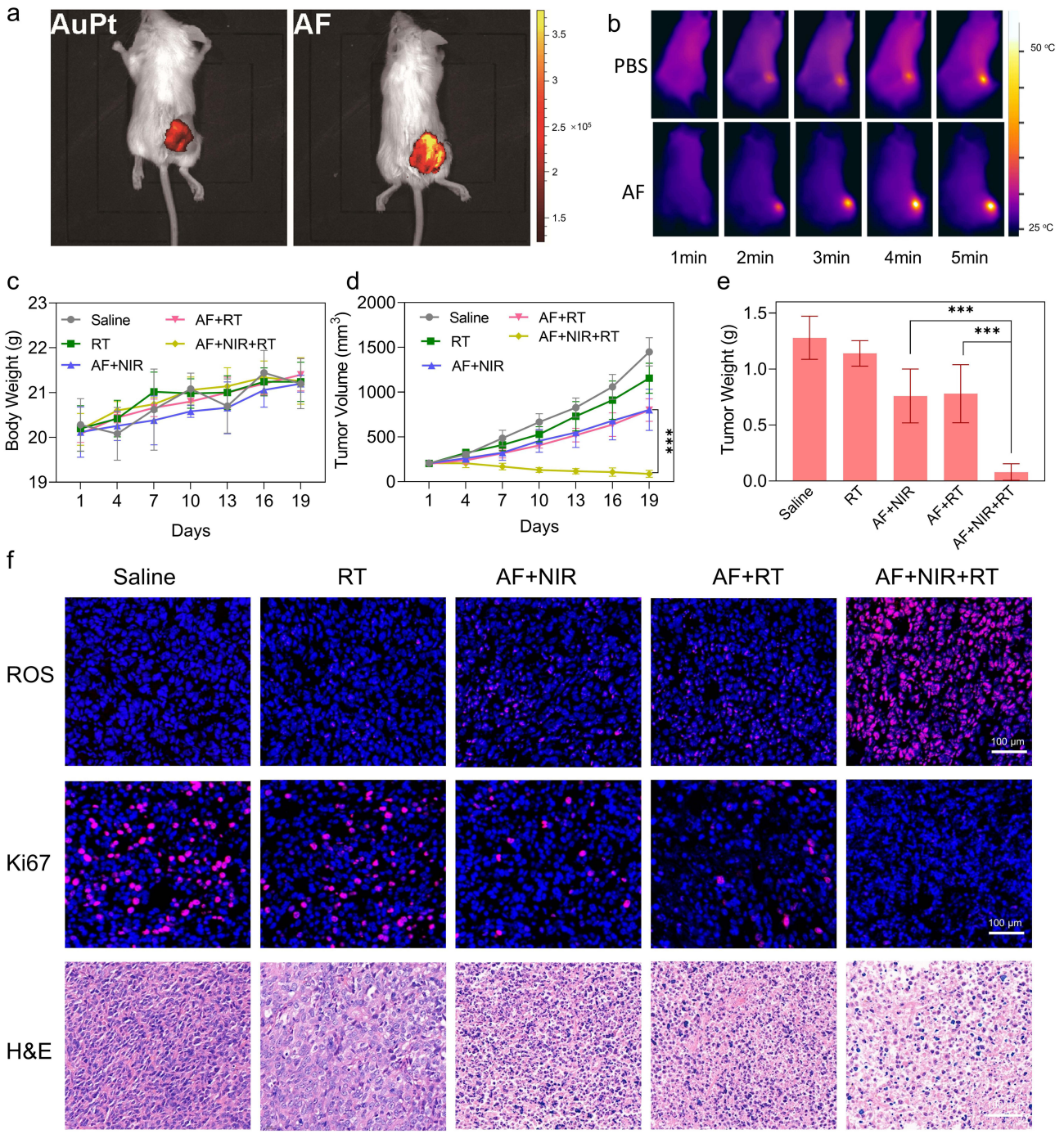

Figure 5 (**a**) IVIS imaging of mice 4 h after AF and AuPt injection. (**b**) Real-time photothermal images. (**c**) Body weight curves. Data points represent mean ± s.d. (n = 5). (**d**) Tumor volume for the five groups. (**e**) Tumor weight curves. Data points represent mean ± s.d. (n = 5). (**f**) ROS, KI67, and H&E staining of the tumor area. Statistical significance was evaluated using an unpaired Student's *t*-test. ***p < 0.001.

group. After 19 days, the mice were euthanized and the tumors were completely removed for morphological analysis. The changes in tumor weight in mice also support our findings, as shown in Figure 5e. In order to study the metabolism of AF in mice, blood was drawn at different times (0, 1, 2, 4, 8, 12, and 24h) to measure AF levels after intravenous injection. As shown in Figure S8a, the AF content in mice decreased by nearly half after about 4h. In addition, after the mice were euthanized, the AF content in various organs including heart, liver, spleen, lung, kidney and tumor was examined, and it was found that the AF was mainly concentrated in the liver (Figure S8b).

After slicing the tumors, ROS, hematoxylin and eosin staining, and Ki97 were used to analyze the apoptosis and growth of tumor cells (Figure 5f). The results indicated that a large number of tumor cells underwent apoptosis and ROS generation in group AF+NIR+RT, followed by group AF+RT and group AF+NIR, which suggests that AF can enhance the treatment effect for tumors. Additionally, the Ki67 stain revealed that cell growth was significantly inhibited after the synergistic treatment of RT and NIR. Furthermore, blood routine tests (including creatinine (CREA), blood urea nitrogen (BUN), aspartate aminotransferase (AST), and alanine aminotransferase (ALT)) were conducted to examine the effects of AF on the mice, and no significant changes were observed compared to the control group (Figure S9).

Conclusion

In this work, we synthesized novel AuPt nanoparticles in a single step and demonstrated their potential for combined RT and PTT treatment. These nanoparticles were smaller in size than conventional ones, resulting in better photothermal conversion and CAT enzyme activity. Additionally, we modified the nanoparticles with FA, which allowed for the accurate targeting of cancer cells. In both in vitro and in vivo experiments, AF exhibited good biocompatibility and excellent photothermal and radiotherapy performance. We also found that AF alleviated hypoxia by catalysing the overexpression of H_2O_2 in the TME, which significantly improved the therapeutic effect on tumours. In summary, our results suggest that AF has great promise for cancer RT and PTT.

Acknowledgments

Han Tang and Ji Chen contributed equally to this work. This project was supported by grants from the National Science Foundation of China (11774272). Thank you to Dr. Chen Nandi for her contribution in studying the pharmacokinetics and biological distribution of radiosensitizers, as well as assisting in completing colony formation experiments.

Disclosure

The authors declare that there are no conflicts of interest related to this article.

References

1. Song G, Cheng L, Chao Y, Yang K, Liu Z. Emerging nanotechnology and advanced materials for cancer radiation therapy. *Adv Mater*. 2017;29(32). doi:10.1002/adma.201700996
2. Yang B, Chen Y, Shi J. Reactive oxygen species (ROS)-based nanomedicine. *Chem Rev*. 2019;119(8):4881–4985. doi:10.1021/acs.chemrev.8b00626
3. Chong Y, Ning J, Min S, Ye J, Ge C. Emerging nanozymes for potentiating radiotherapy and radiation protection. *Chin Chem Lett*. 2022;33(7):3315–3324. doi:10.1016/j.cclet.2022.03.054
4. Zhu D, Lyu M, Huang Q, et al. Stellate plasmonic exosomes for penetrative targeting tumor NIR-II thermo-radiotherapy. *ACS Appl Mater Interfaces*. 2020;12(33):36928–36937. doi:10.1021/acsami.0c09969
5. Liu X, Zhang X, Zhu M, et al. PEGylated Au@Pt nanodendrites as novel theranostic agents for computed tomography imaging and photothermal/radiation synergistic therapy. *ACS Appl Mater Interfaces*. 2017;9(1):279–285. doi:10.1021/acsami.6b15183
6. Dai Q, Wang L, Ren E, et al. Ruthenium-based metal-organic nanoradiosensitizers enhance radiotherapy by combining ROS generation and CO gas release. *Angew Chem Int Ed Engl*. 2022;61(50):e202211674. doi:10.1002/anie.202211674
7. Lyu M, Zhu D, Duo Y, Li Y, Quan H. Bimetallic nanodots for tri-modal CT/MRI/PA imaging and hypoxia-resistant thermoradiotherapy in the NIR-II biological windows. *Biomaterials*. 2020;233:119656. doi:10.1016/j.biomaterials.2019.119656
8. Wu Y, Su L, Yuan M, et al. In vivo X-ray triggered catalysis of H2 generation for cancer synergistic gas radiotherapy. *Angew Chem Int Ed Engl*. 2021;60(23):12868–12875. doi:10.1002/anie.202100002
9. Zhao Z, Gao P, Ma L, Chen T. A highly X-ray sensitive iridium prodrug for visualized tumor radiochemotherapy. *Chem Sci*. 2020;11(15):3780–3789. doi:10.1039/D0SC00862A
10. Cheng L, Shen S, Shi S, et al. FeSe(2)-decorated Bi(2)Se(3) nanosheets fabricated via cation exchange for chelator-free (64)Cu-labeling and multimodal image-guided photothermal-radiation therapy. *Adv Funct Mater*. 2016;26(13):2185–2197. doi:10.1002/adfm.201504810
11. Li J, Zhu D, Ma W, et al. Rapid synthesis of a Bi@ZIF-8 composite nanomaterial as a near-infrared-II (NIR-II) photothermal agent for the low-temperature photothermal therapy of hepatocellular carcinoma. *Nanoscale*. 2020;12(32):17064–17073. doi:10.1039/D0NR03907A
12. Alamdari SG, Amini M, Jalilzadeh N, et al. Recent advances in nanoparticle-based photothermal therapy for breast cancer. *J Control Release*. 2022;349:269–303. doi:10.1016/j.jconrel.2022.06.050
13. Zhi D, Yang T, O'Hagan J, Zhang S, Donnelly RF. Photothermal therapy. *J Control Release*. 2020;325:52–71. doi:10.1016/j.jconrel.2020.06.032
14. Huang C, Liu Z, Chen M, et al. Tumor-derived biomimetic nanozyme with immune evasion ability for synergistically enhanced low dose radiotherapy. *J Nanobiotechnology*. 2021;19(1):457. doi:10.1186/s12951-021-01182-y
15. Yu W, Sun J, Wang X, et al. Boosting cancer immunotherapy via the convenient A2AR inhibition using a tunable nanocatalyst with light-enhanced activity. *Adv Mater*. 2021;34:e2106967.

16. Lu N, Fan W, Yi X, et al. Biodegradable hollow mesoporous organosilica nanotheranostics for mild hyperthermia-induced bubble-enhanced oxygen-sensitized radiotherapy. *ACS Nano*. 2018;12(2):1580–1591. doi:10.1021/acsnano.7b08103
17. Shao F, Wu Y, Tian Z, Liu S. Biomimetic nanoreactor for targeted cancer starvation therapy and cascade amplificated chemotherapy. *Biomaterials*. 2021;274:120869. doi:10.1016/j.biomaterials.2021.120869
18. Zhong D, Li W, Qi Y, He J, Zhou M. Photosynthetic biohybrid nanoswimmers system to alleviate tumor hypoxia for FL/PA/MR imaging-guided enhanced radio-photodynamic synergetic therapy. *Adv Funct Mater*. 2020;30(17):1910395.
19. Chen YZ, Wang ZU, Wang H, Lu J, Yu SH, Jiang HL. Singlet oxygen-engaged selective photo-oxidation over Pt nanocrystals/porphyrinic MOF: the roles of photothermal effect and Pt electronic state. *J Am Chem Soc*. 2017;139(5):2035–2044. doi:10.1021/jacs.6b12074
20. Qin X, Yang C, Xu H, et al. Cell-derived biogenetic gold nanoparticles for sensitizing radiotherapy and boosting immune response against cancer. *Small*. 2021;17(50):e2103984. doi:10.1002/smll.202103984
21. Huang C, Zhang T, Li Y, et al. Type-I AIE photosensitizer triggered cascade catalysis system for tumor targeted therapy and postoperative recurrence suppression. *Chem Eng J*. 2022;446:136381. doi:10.1016/j.cej.2022.136381
22. Chen G, Jiang D, Ding S, Huang C, Zhu D, Jiang H. A tumor cell exosome-mimicking multifunctional nanozyme for targeted breast cancer radiotherapy. *Nanoscale*. 2023;15(36):14949–14957. doi:10.1039/D3NR03065B
23. Yong T, Zhang X, Bie N, et al. Tumor exosome-based nanoparticles are efficient drug carriers for chemotherapy. *Nat Commun*. 2019;10(1):3838. doi:10.1038/s41467-019-11718-4
24. Zhao R, Liu H, Li Y, Guo M, Zhang XD. Catalytic nanozyme for radiation protection. *Bioconjug Chem*. 2021;32(3):411–429. doi:10.1021/acs.bioconjchem.0c00648
25. Garcia-Peiro JI, Bonet-Aleta J, Santamaria J, Hueso JL. Platinum nanoplatforms: classic catalysts claiming a prominent role in cancer therapy. *Chem Soc Rev*. 2022;51(17):7662–7681. doi:10.1039/D2CS00518B
26. Ai Y, Hu ZN, Liang X, Sun H, Xin H, Liang Q. Recent advances in nanozymes: from matters to bioapplications. *Adv Funct Mater*. 2022;32(14):2110432.
27. Xing R, Liu K, Jiao T, et al. An injectable self-assembling collagen-gold hybrid hydrogel for combinatorial antitumor photothermal/photodynamic therapy. *Adv Mater*. 2016;28(19):3669–3676. doi:10.1002/adma.201600284
28. Yang Y, Chen M, Wu Y, et al. Ultrasound assisted one-step synthesis of Au@Pt dendritic nanoparticles with enhanced NIR absorption for photothermal cancer therapy. *RSC Adv*. 2019;9(49):28541–28547. doi:10.1039/C9RA04286E
29. Sun J, Wang J, Hu W, et al. A porous bimetallic Au@Pt core-shell oxygen generator to enhance hypoxia-dampened tumor chemotherapy synergized with NIR-II photothermal therapy. *ACS Nano*. 2022. doi:10.1021/acsnano.2c02528
30. Zhang A, Zhang Q, Alfranca G, et al. GSH-triggered sequential catalysis for tumor imaging and eradication based on star-like Au/Pt enzyme carrier system. *Nano Res*. 2020;13(1):160–172. doi:10.1007/s12274-019-2591-5
31. Wang M, Chang M, Zheng P, et al. A noble AuPtAg-GOx nanozyme for synergistic tumor immunotherapy induced by starvation therapy-augmented mild photothermal therapy. *Adv Sci (Weinh)*. 2022;9(31):e2202332. doi:10.1002/advs.202202332
32. Song Y, Qu Z, Li J, et al. Fabrication of the biomimetic DOX/Au@Pt nanoparticles hybrid nanostructures for the combinational chemo/photothermal cancer therapy. *J Alloys Compd*. 2021;881:160592. doi:10.1016/j.jallcom.2021.160592
33. Kumar A, Singh KRB, Ghate MD, Lalhlenmawia H, Kumar D, Singh J. Bioinspired quantum dots for cancer therapy: a mini-review. *Mater Lett*. 2022;313:131742. doi:10.1016/j.matlet.2022.131742
34. Moglianetti M, De Luca E, Pedone D, et al. Platinum nanozymes recover cellular ROS homeostasis in an oxidative stress-mediated disease model. *Nanoscale*. 2016;8(6):3739–3752. doi:10.1039/C5NR08358C
35. Li P, Liu L, Lu Q, et al. Ultrasmall MoS2 nanodots-doped biodegradable SiO2 nanoparticles for clearable FL/CT/MSOT imaging-guided PTT/PDT combination tumor therapy. *ACS Appl Mater Interfaces*. 2019;11(6):5771–5781. doi:10.1021/acsami.8b18924
36. Oladipo AO, Iku SII, Ntwasa M, Nkambule TTI, Mamba BB, Msagati TAM. Doxorubicin conjugated hydrophilic AuPt bimetallic nanoparticles fabricated from Phragmites australis: characterization and cytotoxic activity against human cancer cells. *J Drug Deliv Sci Technol*. 2020;57. doi:10.1016/j.jddst.2020.101749
37. Song Y, Shi Q, Zhu C, et al. Mitochondrial-targeted multifunctional mesoporous Au@Pt nanoparticles for dual-mode photodynamic and photothermal therapy of cancers. *Nanoscale*. 2017;9(41):15813–15824. doi:10.1039/C7NR04881E
38. Cai R, Xiang H, Yang D, et al. Plasmonic AuPt@CuS heterostructure with enhanced synergistic efficacy for radiophotothermal therapy. *J Am Chem Soc*. 2021;143(39):16113–16127. doi:10.1021/jacs.1c06652
39. Yang S, Han G, Chen Q, et al. Au-Pt nanoparticle formulation as a radiosensitizer for radiotherapy with dual effects. *Int J Nanomedicine*. 2021;16:239–248. doi:10.2147/IJN.S287523
40. Sun P, Hai J, Sun S, et al. Aqueous stable Pd nanoparticles/covalent organic framework nanocomposite: an efficient nanoenzyme for colorimetric detection and multicolor imaging of cancer cells. *Nanoscale*. 2020;12(2):825–831. doi:10.1039/C9NR08486J
41. Ataee-Esfahani H, Wang L, Yamauchi Y. Block copolymer assisted synthesis of bimetallic colloids with Au core and nanodendritic Pt shell. *Chem Commun (Camb)*. 2010;46(21):3684–3686. doi:10.1039/c001516d
42. Xie S, Choi SI, Lu N, et al. Atomic layer-by-layer deposition of Pt on Pd nanocubes for catalysts with enhanced activity and durability toward oxygen reduction. *Nano Lett*. 2014;14(6):3570–3576. doi:10.1021/nl501205j
43. Bian T, Zhang H, Jiang Y, et al. Epitaxial growth of twinned Au-Pt core-shell star-shaped decahedra as highly durable electrocatalysts. *Nano Lett*. 2015;15(12):7808–7815. doi:10.1021/acs.nanolett.5b02960
44. Cheng X, Sun R, Yin L, Chai Z, Shi H, Gao M. Light-triggered assembly of gold nanoparticles for photothermal therapy and photoacoustic imaging of tumors in vivo. *Adv Mater*. 2017;29(6). doi:10.1002/adma.201604894
45. Yuan M, Liang S, Yang L, et al. Rational design of platinum-bismuth sulfide Schottky heterostructure for sonocatalysis-mediated hydrogen therapy. *Adv Mater*. 2022;35:e2209589.
46. Meng X, Zhang J, Sun Z, et al. Hypoxia-triggered single molecule probe for high-contrast NIR II/PA tumor imaging and robust photothermal therapy. *Theranostics*. 2018;8(21):6025–6034. doi:10.7150/thno.26607
47. Chechetka SA, Yu Y, Zhen X, Pramanik M, Pu K, Miyako E. Light-driven liquid metal nanotransformers for biomedical theranostics. *Nat Commun*. 2017;8:15432. doi:10.1038/ncomms15432

48. Gao F, Sun M, Xu L, Liu L, Kuang H, Xu C. Biocompatible cup-shaped nanocrystal with ultrahigh photothermal efficiency as tumor therapeutic agent. *Adv Funct Mater*. 2017;27(24). doi:10.1002/adfm.201700605
49. Liu Q, Fan T, Zheng Y, et al. Immunogenic exosome-encapsulated black phosphorus nanoparticles as an effective anticancer photo-nanovaccine. *Nanoscale*. 2020;12(38):19939–19952. doi:10.1039/D0NR05953F
50. Wang X, Fan L, Cheng L, et al. Biodegradable nickel disulfide nanozymes with GSH-depleting function for high-efficiency photothermal-catalytic antibacterial therapy. *iScience*. 2020;23(7):101281. doi:10.1016/j.isci.2020.101281
51. Lourenco LM, Pereira PM, Maciel E, et al. Amphiphilic phthalocyanine-cyclodextrin conjugates for cancer photodynamic therapy. *Chem Commun (Camb)*. 2014;50(61):8363–8366. doi:10.1039/C4CC02226B